

Dislocation escape-related size effects in single-crystal micropillars under uniaxial compression

H. Tang^a, K.W. Schwarz^b, H.D. Espinosa^{a,*}

^a Department of Mechanical Engineering, Northwestern University, 2145 Sheridan Road, Evanston, IL 60208-3111, USA

^b IBM Watson Research Center, Yorktown Heights, NY 10598, USA

Received 18 September 2006; received in revised form 19 October 2006; accepted 20 October 2006

Available online 27 December 2006

Abstract

The size-dependence of the plastic response of single-crystal micropillars at submicron/micron length scales under compression was investigated using three-dimensional discrete dislocation dynamics (DDD) simulations. In the simulations, the initial dislocation configuration consists of randomly distributed Frank–Read-type dislocation sources. The simulation results are compared with a dislocation evolution model for geometrically confined systems with free surfaces, intended to approximate the evolution behavior of the dislocation density at sufficiently high velocities or stress levels. The dependence of the effective stress on both the sample dimension and source density was shown to take the form $\tau^{\text{eff}} \propto 1/(a\sqrt{\langle N \rangle})$ at a fixed strain rate, where a is the sample dimension and $\langle N \rangle$ is the number density of activated sources. This relationship is found to be in good accord with the DDD simulation results. The new finding in this study is that the size dependence of the plastic response can be independent of source strength in the high-velocity or high-stress regime. The length-scale effects we observe are due to dislocation escape through free surfaces. Mobile dislocations can typically escape faster in a smaller sample, leading to a lower mobile dislocation density and an increased resistance to plastic flow. Thus, the dislocation-escape mechanism provides a possible explanation of the experimentally observed size effects in the testing of micropillars.

© 2006 Acta Materialia Inc. Published by Elsevier Ltd. All rights reserved.

Keywords: Plasticity; Dislocation dynamics; MEMS; NEMS; Nanotechnology

1. Introduction

Metallic materials at micron/submicron length scales exhibit significant size effects when deformed plastically. Fleck et al. [1] showed that, when loaded in torsion, metallic wires display greater strength for smaller radii, while such length-scale effects were not observed in tension. Conventional plasticity theory is incapable of predicting the observed size effects due to the lack of a length scale in the constitutive relations [2]. Emerging gradient plasticity theory appears to be promising and has been successful in explaining some observed size effects related to the presence of geometrically necessary dislocations (GNDs). GNDs can have a dominant effect on the flow stress or

the hardening of metallic materials in the presence of significant plastic-strain or rotation gradients. This can arise even for loading compatible with macroscopically homogeneous deformation due to the constraining of plastic flow by relatively rigid surfaces or substrates [3]. In contrast to the lack of plasticity size effects in tension of a metallic wire [2], significant size effects in free-standing submicron polycrystalline thin films subjected to macroscopically homogeneous fields were first identified by Espinosa et al. [4–6]. These results were recently interpreted by three-dimensional (3-D) discrete dislocation dynamic numerical simulations in Refs. [7–9]. In the studies carried out by Espinosa and co-workers, grain boundary sources were considered, and the size effects were mainly attributed to source-dominated plastic deformation mechanisms.

In the present study, we focus our attention on the understanding of size effects exhibited by geometrically

* Corresponding author.

E-mail address: espinosa@northwestern.edu (H.D. Espinosa).

confined single-crystal systems when plastic deformation is unconstrained. This is motivated by the work of Uchic et al. [10], Dimiduk et al. [11] and Greer et al. [12]. In their studies, compression tests on single-crystal micropillars having diameters ranging from submicron to tens of microns were performed. In Dimiduk et al. [11], single-slip oriented micropillars of pure Ni having sample diameters from 1.0 to 40.0 μm were tested, while multiple-slip-oriented single-crystal micropillars of gold with diameters varying from 0.3 to 7.45 μm were investigated in Ref. [12]. In both studies, the experiments revealed a strong size-dependent material response. The measured flow stresses were significantly higher than that of the material in bulk. A trend of increasing flow stress with decreasing micropillar diameter was observed. In Ref. [12], the “dislocation starvation” mechanism reflected by discrete strain bursts separated by periods of nearly elastic loading was considered as the key to the observed size dependence. According to this mechanism, the free distance that dislocations can travel for breeding is limited by the sample dimensions. As a result, dislocations generally escape from the free surfaces of the single-crystal micropillars prior to multiplication through mechanisms like double cross-slip. This leads to the formation of dislocation-starved conditions responsible for so-called exhaustion hardening. In order to sustain plastic deformation, the applied stress must be increased to elevate the source-operation rate or to activate more “hard” dislocation sources. In Ref. [11], the mechanism related to exhaustion hardening was further elaborated in the context of dislocation kinetics. Plausibly, the authors attributed the observed size effects to three stochastic effects – dislocation generation by a stress-dependent source distribution; dislocation escape at free surfaces; and dislocation trapping, which alters the stress-dependent mobile density and source density.

In order to shed light on the observed size effects, Deshpande et al. [13] modeled the deformation of a planar single crystal under compression using 2-D discrete dislocation plasticity. Both small-strain and finite-deformation analyses were conducted. In Deshpande et al.’s study, results obtained with and without constraining of the tensile axis against rotation were compared. Their results showed that the size dependence was stronger for the latter case, qualitatively consistent with the experimental results. The size effects observed in their study arise primarily from interactions between dislocations and obstacles. In another study, Benzerga and Shaver [14] used mechanism-based discrete dislocation plasticity to investigate size effects on the plastic response of single-crystal micropillars. In their study, the size effects were attributed to the internal stresses as well as to the source strength and time scales associated with source nucleation.

While 2-D dislocation-plasticity modeling provides useful insights into the experimentally observed size effects, there are a number of idealizations that require further study. In a 2-D model, the effect of dislocation curvature is ignored. Moreover, the importance of long-range inter-

actions is overestimated, and several key 3-D dislocation interaction mechanisms must be either ignored or added in an ad hoc manner. In the present study, a completely 3-D approach is used to investigate the effect of dislocation escape on the size-dependent plastic response of micropillars under uniaxial compression. While it has been believed that dislocation escape plays a significant role on the experimentally observed size effects, the details of the operating mechanisms associated with dislocation escape have not been fully investigated.

Our paper is organized as follows. In Section 2, we briefly review the discrete dislocation dynamics model used in the calculations. In Section 3, we then define the problems to be examined. Both simulation results and mathematical models are presented in Section 4. Some concluding remarks on this study are given in Section 5.

2. Discrete dislocation dynamics model

The simulations conducted here use the code PARANOID. Details on the methods used in PARANOID were described in Refs. [15,16]. Here we briefly review some important features of the discrete dislocation dynamics (DDD) methods used in this study.

In the DDD model, the motion of dislocation lines determines the plastic deformation of a crystal. While the detailed microscopic nature of the dislocation core region fixes specific dislocation parameters such as the slip system, the effective core radius and the drag coefficient, the idea of DDD is to treat the dislocations as line singularities in an elastic continuum. To calculate their behavior, each dislocation line is represented by a chain of nodal points. The glide force per unit length acting at each node is then determined from the Peach–Koehler relation:

$$\mathbf{f}_g = (\mathbf{b} \cdot \boldsymbol{\sigma}^T \cdot \mathbf{n}) \mathbf{n} \times \mathbf{t} \quad (1)$$

where \mathbf{b} is the Burgers vector of the dislocation, $\boldsymbol{\sigma}^T$ is the total stress tensor, \mathbf{n} is the normal to the slip plane and \mathbf{t} is the unit vector pointing in the direction of the line segment. The total stress tensor includes the applied stresses and the internal stresses generated by the presence of dislocation themselves. Since the solutions for the internal stress field are obtained for an infinite body, additional corrections are required for satisfying boundary conditions. To maintain stability of computation, the core-splitting is generally continued beyond the nearest neighboring nodes. Once the force at each node is determined, the node is moved according to the viscous drag rule

$$\mathbf{V} = \mathbf{f}_g / B \quad (2)$$

where B is the drag coefficient. No thermally activated process is taken into account in the calculations.

Dislocation escape occurs when dislocation lines intersect a free surface. In principle, the interaction of the dislocations in our sample with its free surfaces is an extremely demanding computational problem. A detailed examination [17] of this issue has, however, shown that very simple

approximations work surprisingly well for situations in which the dislocation lines have significant curvature. Accordingly, in the present calculations any dislocation encountering a free surface simply reconnects to the surface, after which the ends are allowed to move freely along the surface. All other surface corrections are neglected. As demonstrated by Liu and Schwarz [17], this leads to relatively small errors, of the order of 10%. To this degree, the effects of image forces on the evolution of total dislocation density of a crystal sample are not considered as significant. In particular, for cases where the sources are overstressed for a rapid multiplication or source operation rate, the effects of image forces can become trivial on the material response. For example, this can occur in the compression tests of single-crystal pillars with diameters below $\sim 10 \mu\text{m}$. In these tests, plastic flow takes place under significantly higher applied stress compared with macroscopic crystals [11]. Thus, the dislocations inside these small samples are most likely to be overdriven by the applied stress.

In the calculations conducted here, the macroscopic plastic strain rate is computed from the relation

$$\dot{\epsilon}^p = \frac{1}{2V} \sum_{i=1}^M l_i^\alpha v_i^\alpha (\mathbf{b} \otimes \mathbf{n}^\alpha + \mathbf{n}^\alpha \otimes \mathbf{b}) \quad (3)$$

where V is the volume of the simulated crystal, l_i^α is the length of dislocation segment i moving on the slip plane α , v_i^α is the corresponding moving velocity of the segment and M is the total number of dislocation segments.

3. Problem definition

The geometry of the single-crystal micropillar used in the simulations is illustrated in Fig. 1. As noted, a square cross-section is considered here in contrast to the circular cross-section of micropillars tested in the experiments.

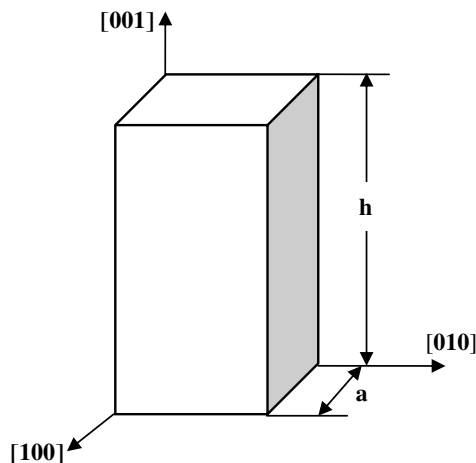


Fig. 1. Schematic of an fcc single-crystal micropillar with square cross-section oriented in the [001] direction. Axial compression was imposed along the [001] direction. A constant aspect ratio $h/a = 3$ was used in all the simulations.

Limited studies performed on similar pillars but with circular cross-sections indeed showed that the cross-sectional shape plays a trivial role on the simulation results. The aspect ratio h/a between the height of the micropillar and the side length is fixed at 3.0, and only uniaxial compression in the [001] direction is considered. Frank–Read sources are randomly distributed through the volume, and are assigned a Gaussian distribution of lengths. All twelve $\langle 011 \rangle \{111\}$ slip systems of an face-centered cubic (fcc) crystal are considered in the calculations. However, only eight of them can be activated when the pillar is loaded along the [001] crystal orientation. Here the total number of activated sources belonging to the eight slip systems is denoted by N . Unless stated otherwise, each slip system has the same number of sources.

The single crystal is taken to be elastically isotropic, with an elastic shear modulus $\mu = 42.3 \text{ GPa}$ and a Poisson ratio $\nu = 0.3$. A Burgers vector magnitude $b = 0.26 \text{ nm}$ is used in the calculations. The material response of the single-crystal micropillars was modeled both under creep conditions and with fixed ends (relaxation). In the modeling of the latter case, the strain is applied instantly such that the initial dislocation configurations are not influenced by the loading process. The response of micropillars under compression with a fixed strain rate $\dot{\epsilon} = -6.66 \times 10^5 \text{ s}^{-1}$ was also simulated. The effect of strain rate on this type of calculation was discussed in Ref. [9]. Although inertial effects are expected to come into play at such a high strain rate, no attempt has been made to include the related physical mechanisms in the present study. In addition, the velocity dependence of mobility [18] in the high-velocity regime is ignored here; that is, the mobility or viscous drag coefficient is taken to be a constant.

4. Results and discussion

4.1. Size effects on dislocation density evolution

In this section, we study the mechanisms controlling the size dependence of dislocation-density evolution under creep conditions. We first present a mathematical model characterizing the evolution of the dislocation density. The model is then compared with the results obtained from three-dimensional DDD simulations.

4.1.1. Evolution of dislocation density in geometrically confined systems with free surfaces

The evolution of the mobile-dislocation density in a body with free surfaces takes the form [19]:

$$\dot{\rho}_m = \dot{\rho}_{\text{mul}} - \dot{\rho}_{\text{tr}} - \dot{\rho}_{\text{esc}} \quad (4)$$

where $\dot{\rho}_m$ is the rate of change in the mobile-dislocation density, $\dot{\rho}_{\text{mul}}$ is the dislocation multiplication rate, $\dot{\rho}_{\text{tr}}$ is the rate at which dislocations are trapped per unit volume, and $\dot{\rho}_{\text{esc}}$ is the dislocation-escape rate through the free surfaces. The total dislocation-density evolution rate is given as the sum of the mobile and trapped density rates,

$$\dot{\rho}_t = \dot{\rho}_m + \dot{\rho}_{tr}. \quad (5)$$

In the study conducted here, $\dot{\rho}_{tr}$ is mainly attributed to dislocation trapping by dipoles, forest dislocations or jog formation through collinear interaction [20].

A dislocation-multiplication model proposed by Moulin et al. [21] is adapted to include a source density for the single crystal considered here. It is assumed that there exist N independently activated sources in the single crystal, and that each of them has emitted an equal number of dislocation loops. Following Moulin et al. [21], the increase of dislocation density produced by these loops during time interval can be expressed as

$$d\rho_{mul} = N\phi n\bar{v}dt/V \quad (6)$$

where ϕ is a geometrical constant, \bar{v} is the dislocation velocity and n is the number of loops emitted by each source and remaining in the crystal. The total mobile-dislocation density is related to n by

$$\rho_m = \frac{N\phi}{V} \sum_{i=1}^n i\Delta e \approx \frac{N\phi\Delta e}{2V} n^2 \quad (7)$$

where Δe is the spacing between loops. It is shown that the spacing Δe is approximately proportional to the inverse of the effective stress, $1/\tau^{\text{eff}}$, stemming from the influence of the linear velocity–stress law [21,22]. The effective stress is defined as the total stress resolved in the active slip system. Combining Eq. (6) with Eq. (7), we have

$$\dot{\rho}_{mul} = k\bar{v}\sqrt{2\phi\langle N\rangle\tau^{\text{eff}}}\rho_m \quad (8)$$

where $\langle N\rangle = N/V$ is the number density of activated sources and k is a constant.

The dislocation escape rate through the free surfaces is related to the dislocation flux by

$$\dot{\rho}_{esc} = \delta_e \frac{\rho_m \bar{v}}{l} \quad (9)$$

where l is a characteristic dimension in the slip direction and δ_e is a geometrical constant.

The steady regime is characterized by $\dot{\rho}_m = 0$, which occurs when the loss of mobile dislocations through both dislocation escape and trapping is compensated by dislocation multiplication. In the high-stress or high-velocity regime, the formation of dislocation junctions or dipoles is expected to be restricted because the externally applied high stress can easily destroy the weaker junctions or dipoles. In this study, we define the high-stress regime as that in which the applied stress resolved in the active slip system is at least twice as large as the average source-activation stress [23], $\tau^{\text{cr}} = \mu b/\bar{L}$, where \bar{L} is the average source length. We assume that the immobile-dislocation storage in a confined volume through forest or dipole trapping can be neglected in the high-stress regime. As a result, in the steady-state regime we have

$$\dot{\rho}_{mul} = \dot{\rho}_{esc}. \quad (10)$$

Combining Eqs. (8)–(10), the mobile-dislocation density at steady state takes the form

$$\rho_m = k_1 l^2 \langle N \rangle \tau^{\text{eff}} \quad (11)$$

where $k_1 = 2k^2\phi/\delta_e^2$ is a combined geometrical constant. The relationship reveals that at steady state there is a linear dependence of the mobile-dislocation density on the effective stress, on the density of sources, and on the square of the characteristic dimension in the slip direction. It is emphasized that the use of Eq. (11) is subjected to the restrictions of a fixed number of sources, the linear velocity–stress law and planar glide dominating the plastic deformation. In addition, the relationship is more acceptable in the high-stress or high-velocity regime. In this regime, the effective stress is assumed to be approximately equal to the externally applied stress resolved into the active slip system.

4.1.2. Comparison with simulation results

In this subsection, we discussed the computed creep responses of micropillars. The simulations were carried out following the methods described in Section 2 to the system defined in Section 3. As illustrated in Fig. 2, the linear dependence of the steady-state dislocation densities on both the applied stress and the source density $\langle N\rangle$ predicted by Eq. (11) is in accord with our simulation results.

Before the steady-state regime is achieved, the dislocation density in the crystal is expected to increase continuously according to the source model we use here. This is illustrated in Fig. 3, which shows the evolution of dislocation density with time in units of B/μ for the applied stresses $\sigma = 450$ MPa and 650 MPa. In these calculations, a micropillar with a side dimension $a = 0.4$ μm was considered. A total of 64 activated Frank–Read-type dislocation sources, with average source length $\bar{L} = 0.1$ μm and standard deviation $\delta = 0.02$ μm were used in the simulations.

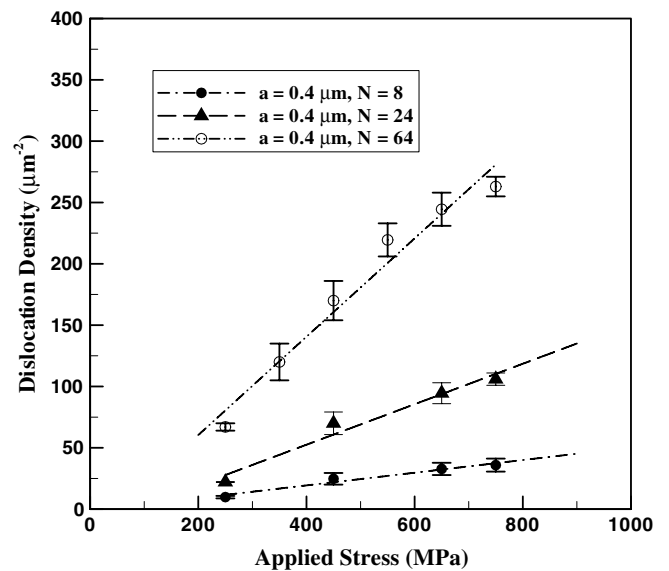


Fig. 2. Dislocation density as a function of applied stress, for different numbers of sources, in the steady-state regime. A linear dependence of dislocation density on both the applied stresses and source numbers is revealed.

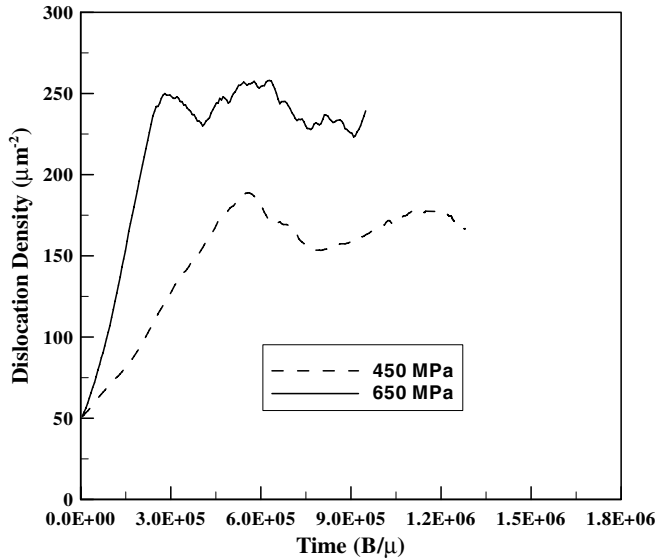


Fig. 3. Dislocation-density histories for the case $a = 0.4 \mu\text{m}$ at different stress levels during pillar compression. A total of 64 activated Frank–Read sources with source strength characterized by a Gaussian distribution was employed. The average source size was $\bar{L} = 0.1 \mu\text{m}$ and the standard deviation $\delta = 0.02 \mu\text{m}$. The density of activated sources $\langle N \rangle$ was kept constant.

As shown in Fig. 3, both the transient and steady-state regimes can be clearly identified. In the transient regime, the dislocation density increases continuously with increasing plastic strain. Once the dislocation lines intersect the surfaces, a steady-state regime is established. This regime is characterized by simultaneous dislocation multiplication and escape. The dislocation density at steady state is shown to increase with increasing applied stress, in agreement with the model leading to Eq. (11).

We also performed DDD simulations to examine the effect of pillar size, a , on the steady-state dislocation density. The results are shown in Fig. 4. In this plot, the steady-state dislocation density versus the applied stress are compared for the two cases $a = 0.2 \mu\text{m}$ and $0.4 \mu\text{m}$. The initial densities of activated sources, $\langle N \rangle$, are taken to be the same for both cases, with $N = 8$ when $a = 0.2 \mu\text{m}$ and $N = 64$ when $a = 0.4 \mu\text{m}$. In both cases, the source lengths are assigned to have values in terms of a Gaussian distribution with average source length $\bar{L} = 0.1 \mu\text{m}$ and standard deviation $\delta = 0.02 \mu\text{m}$. The slope of the fitted line for the case with the larger sample size is shown to be approximately four times that for the case with the smaller sample size, see Fig. 4. This is again consistent with the relationship described by Eq. (11), in which the slope is proportional to l^2 . Note that the length l in the slip direction is proportional to the sample dimension.

Another feature revealed by the simulations is that the mobile-dislocation density in the large sample is higher than that in the small sample due to the relatively fast dislocation escape in the latter (Fig. 4). As a result, we expect the plastic strain rate in the larger sample to be higher than that in the smaller sample under the same applied stress.

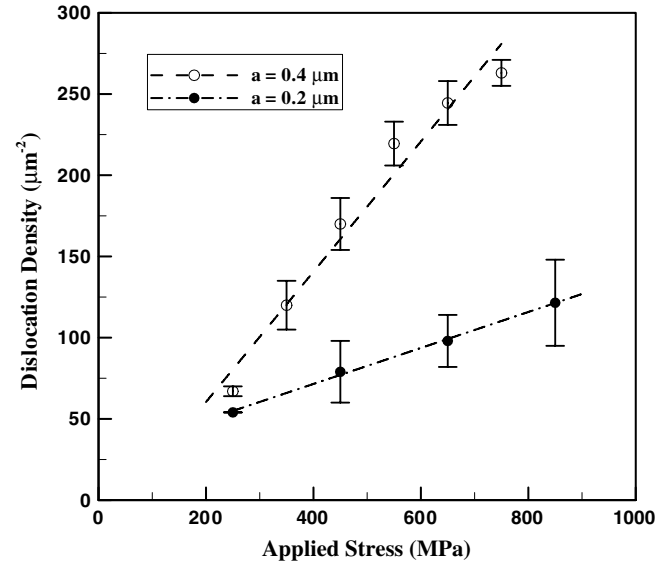


Fig. 4. Dislocation density as a function of the applied stress, in the steady-state regime, for the cases $a = 0.2 \mu\text{m}$ and $0.4 \mu\text{m}$, respectively. A linear dependence of dislocation density on both the applied stress and the square of the cross-sectional dimension is revealed.

This is clearly revealed in Fig. 5 for a constant stress of 600 MPa.

4.2. Effects of dislocation escape on stress relaxation

Size-scale effects on stress relaxation were also investigated. Simulations were carried out for an applied strain $\varepsilon = 0.5\%$, using $a = 0.2 \mu\text{m}$ and $0.4 \mu\text{m}$. The initial dislocation configurations and densities are the same as those used to obtain Fig. 4. In Fig. 6a and b, the evolution of the

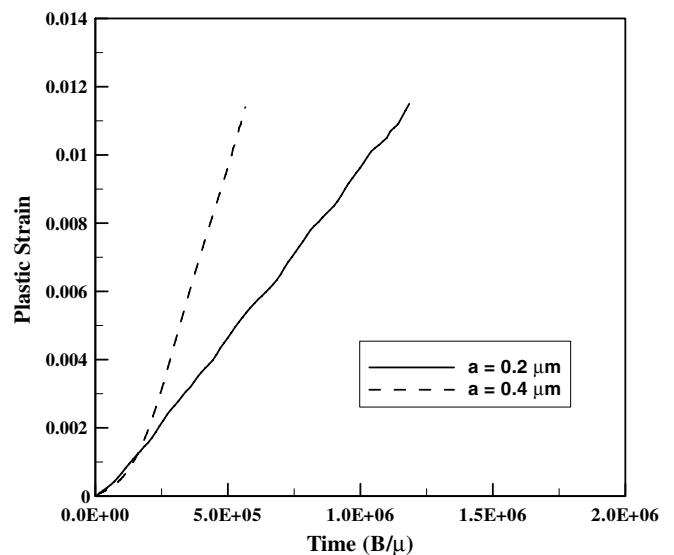


Fig. 5. Plastic strain history under constant stress $\sigma = 600 \text{ MPa}$ for the cases $a = 0.2 \mu\text{m}$ and $0.4 \mu\text{m}$, respectively. The plastic strain rate for the larger sample is higher than that for the smaller sample due to the dislocation-escape mechanism.

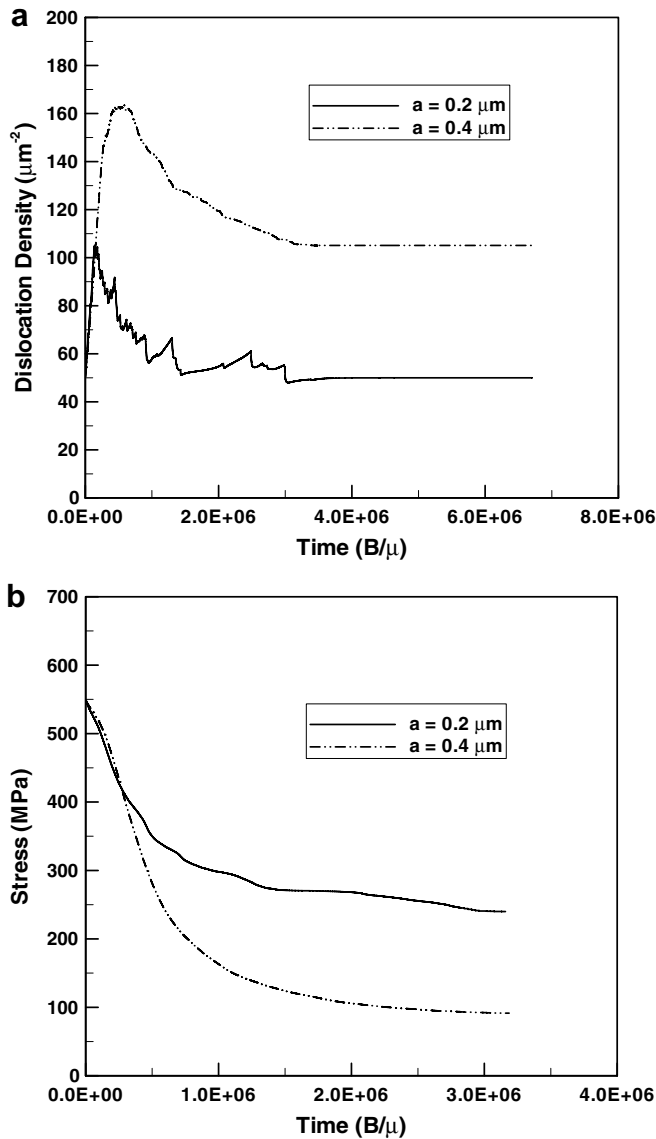


Fig. 6. (a) Dislocation density and (b) stress histories for the cases $a = 0.2 \mu\text{m}$ and $0.4 \mu\text{m}$. Simulations were performed at a fixed strain $\varepsilon = 0.5\%$.

mobile dislocation density and stress level are displayed for the two samples. Both the density growth and the stress relaxation rate are initially the same in both samples. However, dislocations reach the surface earlier in the smaller sample, after which the dislocation density decreases as the continued relaxation of the internal stress lowers the dislocation multiplication rate.

A noteworthy feature of Fig. 6b is that the equilibrium stress level for the small sample differs significantly from that for the large sample. The equilibrium stress at full relaxation for the former appears to be close to the applied stress required for source activation, which is estimated as $\sigma = \tau^{\text{cr}}/M$, where $M = 1/\sqrt{6}$ is the Schmid factor for loading in the $[001]$ direction. With $\bar{L} = 0.1 \mu\text{m}$ and $\tau^{\text{cr}} = \mu b/\bar{L}$, we have $\sigma = 265 \text{ MPa}$, which is close to the stress level at

equilibrium shown in Fig. 6b for $a = 0.2 \mu\text{m}$. For the larger sample, the equilibrium stress level is lower than the level required to activate dislocation sources in the initial configuration. This is due to the fact that Frank–Read sources on the same slip system can recombine via annihilation interactions to produce more extended sources which are easier to activate. In this connection we draw attention to Fig. 7, which shows that the equilibrium state for the $0.2 \mu\text{m}$ sample is similar to the initial state, whereas the $0.4 \mu\text{m}$ sample equilibrium state shows a drastically different structure, exhibiting many long dislocation segments and junctions. Movies showing the evolution of the dislocation structures for each case are given at the URL listed in Ref. [24].

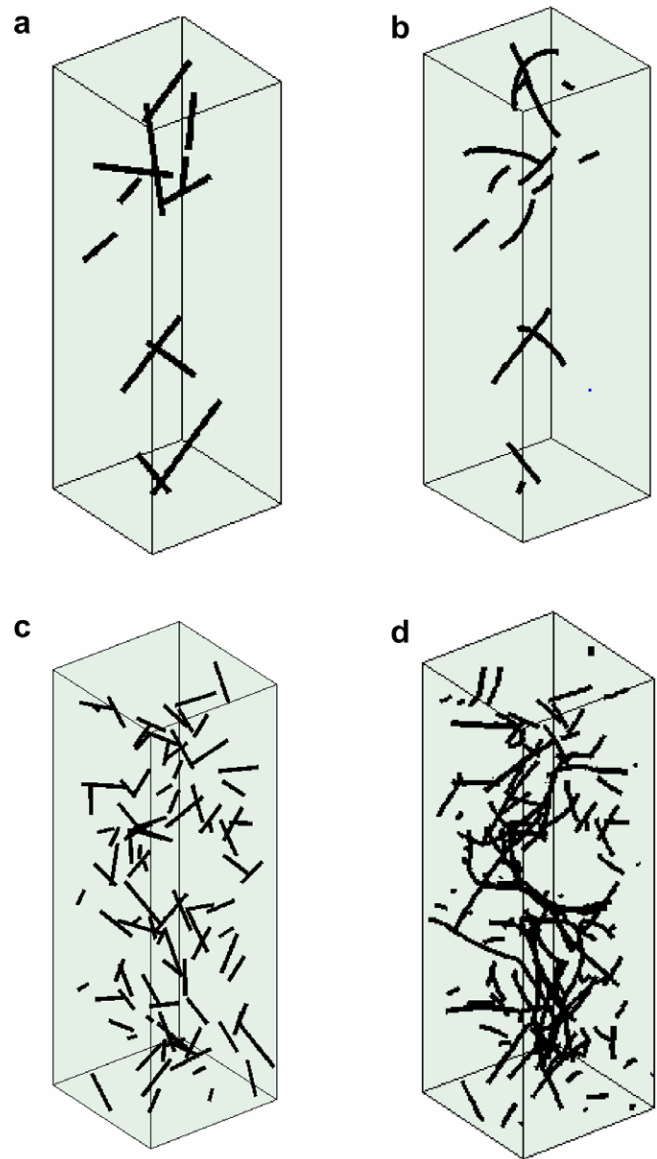


Fig. 7. Dislocation configurations for (a) $a = 0.2 \mu\text{m}$ prior to loading; (b) $a = 0.2 \mu\text{m}$ at equilibrium; (c) $a = 0.4 \mu\text{m}$ prior to loading; and (d) $a = 0.4 \mu\text{m}$ at equilibrium. The average source size used in the simulations was $\bar{L} = 0.1 \mu\text{m}$ and the standard deviation was $\delta = 0.02 \mu\text{m}$.

4.3. Size effects on the stress–strain response at constant strain rate

Having studied the effect of size on dislocation density evolution during creep and stress relaxation, we now examine the same effect on the material stress–strain response at constant strain rate. We begin by examining some relevant constitutive equations.

4.3.1. Mathematical model

Assuming that the elastic strain rate is negligible compared with the plastic strain rate in the presence of stable plastic flow with a fixed strain rate, we have

$$\dot{\epsilon} \approx \dot{\epsilon}^p = \rho_m \bar{v} b \quad (12)$$

where \bar{v} is the average dislocation velocity. As discussed in Ref. [23], the average dislocation velocity approaches the velocity limit in free flight when the applied stress resolved in the active slip system is greater than about twice the critical source-activation stress. In the high-velocity or high-stress regime, the average dislocation velocity becomes approximately proportional to the effective stress, τ^{eff} . Hence, by combining Eqs. (11) and (12) and eliminating ρ_m , the effective stress is shown to take the form

$$\tau^{\text{eff}} = \frac{C\sqrt{\dot{\epsilon}}}{l\sqrt{\langle N \rangle}} \quad (13)$$

where C is a constant. Eq. (13) can further be written as

$$\tau = \tau_i + \frac{C\sqrt{\dot{\epsilon}}}{l\sqrt{\langle N \rangle}} \quad (14)$$

with the effective stress $\tau^{\text{eff}} = \tau - \tau_i$, where τ is the applied stress resolved in the active system and τ_i is related to both short- and long-range dislocation interactions. In the high-velocity or high-stress regime, the effects of τ_i on the flow stress is typically negligible when compared with viscous resistance to plastic flow. Therefore, the relationship described by Eq. (14) shows that the flow stress in micropillars, at a given strain rate, should vary linearly with $1/(l\sqrt{\langle N \rangle})$. This implies that not only the sample dimension but also the source density plays a significant role on the flow stress of micropillars. Obviously, this relationship is subjected to the same restrictions as those for the relationship described by Eq. (11).

4.3.2. Comparison with DDD simulation results

In Fig. 8, the stress–strain response curves for three representative sample sizes $a = 0.4 \mu\text{m}$, $0.6 \mu\text{m}$ and $0.8 \mu\text{m}$ are displayed. The strain rate was held fixed at $\dot{\epsilon} = -6.66 \times 10^5 \text{ s}^{-1}$, and the density of activated sources was held fixed with $\langle N \rangle = 15.625 \mu\text{m}^{-3}$. The average length of sources was taken to have a value $\bar{L} = 0.2 \mu\text{m}$, while the standard deviation was $\delta = 0.04 \mu\text{m}$. As shown in this plot, the pillar hardens as its size is decreased, consistent with Eq. (14). The mobile dislocation density decreases with decreasing sample dimensions because of the dislocation-

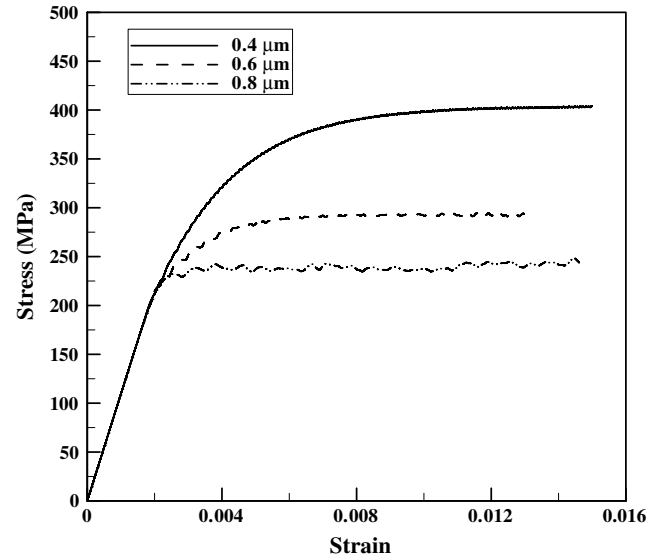


Fig. 8. (a) Stress–strain curves for pillars of various cross-sections. The density of sources was fixed at $\langle N \rangle = 15.625 \mu\text{m}^{-3}$ in the simulations. The average source size was $\bar{L} = 0.2 \mu\text{m}$, with standard deviation $\delta = 0.04 \mu\text{m}$. The strain rate was $\dot{\epsilon} = -6.66 \times 10^5 \text{ s}^{-1}$.

escape mechanism, thereby increasing the resistance to plastic flow.

Simulations for cross-sections with dimensions in the range $a = 0.3\text{--}1.6 \mu\text{m}$ and a fixed number of activated sources were also performed. The source density was varied with sample dimensions, accordingly. We place one dislocation source on each of the eight activated slip systems of the fcc crystal. The average source length was set to $\bar{L} = 0.4 \mu\text{m}$, while the standard deviation was set to $\delta = 0.08 \mu\text{m}$. The responses for pillars with side length varying from 0.3 to $1.6 \mu\text{m}$ are displayed in Fig. 9a. As shown in the plot, cases with a greater than $0.8 \mu\text{m}$ exhibit a quite smooth stress–strain response. This reveals a progressive transition from the linear regime to the nonlinear one. The transition begins with the activation of sources and ends with the establishment of an approximately steady-state plastic regime. Examination of Fig. 9a reveals that the flow stress increases with the increase of sample size. This is attributed to the decrease of the source density with the increase of the sample dimension, noting that the numbers of sources are the same for all the samples. A salient feature revealed by these results is that extremely low hardening is displayed after yielding. Dislocation trapping or immobile-dislocation storage is barely observed in the simulations. The extremely low hardening was also exhibited in the testing of single-crystal micropillars [10].

For cases with a smaller than $0.8 \mu\text{m}$, the stress–strain curves exhibit other features as a result of the discreteness of the dislocation-source activation process and strong interactions between the Frank–Read sources and the free surfaces. Note that, in these cases, the sizes of the Frank–Read sources are close to the sample characteristic dimension a . The distance between the pinning points and the boundaries is then typically smaller than the distances

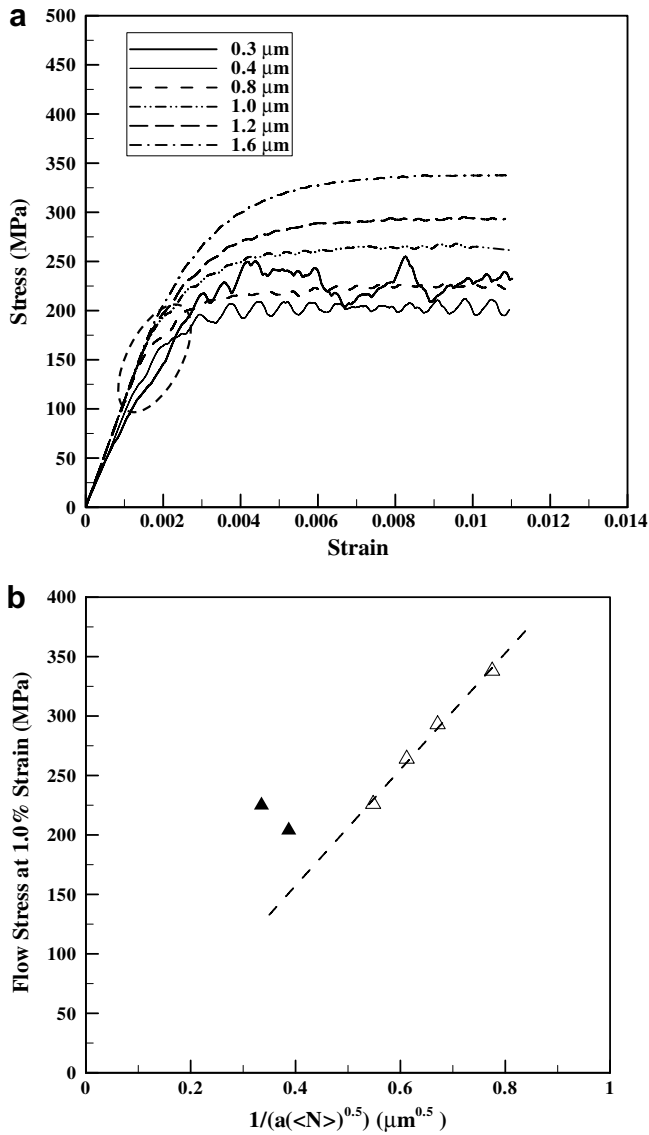


Fig. 9. (a) Stress–strain curves for pillars of various cross-sections. The activated-source number was fixed at 8 in the simulations. The average source size was $\bar{L} = 0.4 \mu\text{m}$, with standard deviation $\delta = 0.08 \mu\text{m}$. For the cases $a = 0.3 \mu\text{m}$ and $a = 0.4 \mu\text{m}$, stress steps are observed in the transition from elasticity to plasticity. (b) The flow stresses at 1.0% strain are shown as a function of $1/(a\sqrt{\langle N \rangle})$. A linear dependence is displayed for cases with relatively large sample sizes. For the cases in which the sample sizes are close to the average dislocation source length, the progressive change of the Frank–Read sources increases the source activation stress, leading to higher flow stress. This is the case for simulation results plotted as solid triangle symbols, $a = 0.3 \mu\text{m}$ and $a = 0.4 \mu\text{m}$.

between pinning points. Therefore, the Frank–Read source develops into a pair of spiral sources under loading [25], and the final source activation stress is actually determined by the distance between the pinning point and the boundary. Such stress can be significantly higher than that for activating the Frank–Read source itself. An interesting feature highlighted by the oval shown in Fig. 9a is the formation of stress steps. This reflects the discontinuity of source operation. Some sources with larger lengths are activated at a lower applied stress, leading to the detectable plastic

flow reflected by the stress steps. However, the operation of these sources gets aborted soon after the first activation due to the proximity of free surfaces. These sources are generally reactivated at a much larger applied stress.

We plot in Fig. 9b the flow stress at 1.0% permanent strain for the responses shown in Fig. 9a as a function of $1/(a\sqrt{\langle N \rangle})$. It is noted that, for cases with sample sizes greater than $0.6 \mu\text{m}$, a linear relationship between the flow stresses $1/(a\sqrt{\langle N \rangle})$ and is revealed. This is in good agreement with the analytical relation described by Eq. (14). For the cases with $a = 0.3 \mu\text{m}$ and $0.4 \mu\text{m}$, however, the flow stresses are higher than those estimated from the linear relationship given by Eq. (14). In these cases, the interactions between dislocations and surfaces modify the value of \bar{L} , as stated earlier. Hence, the critical source-activation stress in these cases indeed becomes larger than that for

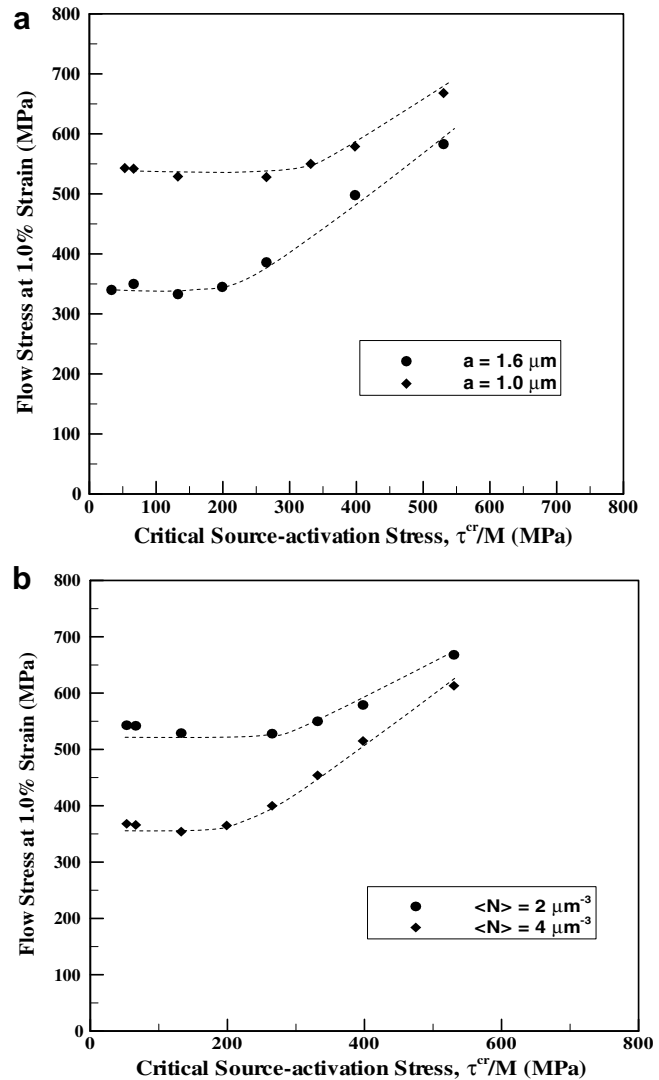


Fig. 10. Flow stress vs. source-activation stress. (a) Effect of characteristic dimension. The activated source density is held fixed to $\langle N \rangle = 2 \mu\text{m}^{-3}$. (b) Effect of the density of activated sources. The sample dimension was held fixed with $a = 1.0 \mu\text{m}$. $M = 1/\sqrt{6}$ is the Schmid factor for the loading direction.

activating an isolated Frank–Read source. For cases with relatively large source strengths, the overall flow stress tends to become source-strength controlled, as discussed next.

4.3.3. Effects of source-activation stress

The dependence of flow stress on source strength was also investigated in this study. In Fig. 10a and b, the relationships between the flow stresses at 1.0% permanent strain and the average source-activation stresses are displayed. Fig. 10a displays the flow stress vs. source-activation stress for two different sample sizes. The densities of activated sources was fixed at $\langle N \rangle = 2 \mu\text{m}^{-3}$. In Fig. 10b, the effects of the number of activated-source densities on the flow stress vs. source activation stress are illustrated. Two cases, $\langle N \rangle = 2$ and $4 \mu\text{m}^{-3}$, are compared for a fixed sample dimension $a = 1.0 \mu\text{m}$. It is noted that two regions can be clearly identified in these two plots. One is the flat region in which the flow stresses are independent of the source-activation stresses. In this region, the applied stresses resolved in the active slip systems are typically more than twice the source-activation stresses. Under this condition, the dislocation average velocity approaches the velocity limit in free flight, which is viscous-drag controlled [23]. The flow stress is dominated by the size- and source density-dependent term on the right-hand side of Eq. (14). In the other region, the applied stresses resolved in the active slip systems become less than twice the source-activation stresses. As a result, the average dislocation velocity can be much smaller than the free-flight velocity limit. In this regime, the flow stresses are shown to increase with increasing source-activation stresses. Size effects on the flow stress are still observed in this region with a decreasing trend. For extremely high source strengths, the flow stress is expected to become entirely source-activation controlled.

5. Concluding remarks

The present study has shown that dislocation escape through free surfaces plays a significant role in the size-dependence of the plastic response of single-crystal micropillars under compression. In terms of the evolution model of dislocation density presented in this study, the mobile-dislocation density at steady state is a linear function of the applied stress, the activated-source density and the sample dimension squared. This is restricted to the high-velocity or high-stress regime for a fixed number of dislocation sources.

The mechanisms dominating the size dependence of the plastic response shown in this study are different from those discussed in Deshpande et al. [13] and Benzerga and Shaver [14]. In Ref. [13], the predicted size effects were attributed to obstacle-limited behavior. Benzerga and Shaver [14] emphasized the importance of the length of sources on the observed size effects. The length of sources generally increases with increasing sample size. Thus, a lower stress is required on average to initiate plastic flow for a larger sam-

ple. Here we show that the size dependence of flow stress can be totally independent of source strength and obstacles in the high-stress or high-velocity regime. For a fixed strain rate, we show mathematically that the flow stress at steady state is related to both the sample dimension and the density of activated sources in terms of the relationship $\sigma \propto 1/(a\sqrt{\langle N \rangle})$. The size-dependent stress–strain response is essentially dominated by the dislocation-escape mechanism.

Since the experimentally observed compressive flow stress in micropillars is significantly larger than that in the bulk crystal, it is reasonable to assume that the plastic deformation behavior exhibited by these micropillars falls in the high-velocity or high-stress regime. Thus, it is possible to use the relationship described by Eq. (14) to explain the experimentally observed size effects. In terms of Eq. (14), the flow stress should scale as $1/a$ for a fixed density of activated sources. This reveals a stronger size effect than that shown in Ref. [11]. One possible explanation that would account for this discrepancy is that the number of activated sources per unit volume for smaller samples is likely larger than that for larger samples. Since the pillars are fabricated by focus ion beam etching of a substrate, statistically it is quite probable that is the case. In addition, other mechanisms related to the stress-dependent dislocation sources which may scale with sample sizes cannot be excluded. The present study has also shown that the flow stress tends to become source-strength controlled with increasing source-activation stress.

In the present study, we are restricted to using a fixed number of sources in the simulations. This excludes the effects of possible source change on the compressive response of micropillars. For example, some sources may be deactivated or exhausted due to the change of source configurations during loading. This will lead to the hardening or even shutting down of the plastic flow. An improved understanding of source operation mechanisms in micropillars under compression appears to be important in order to shed more light on the experimentally observed size effects. This has been a primary goal in our ongoing study. However, we believe that the results from the present study do provide insight into what can be expected to occur in a more complex system.

Acknowledgements

This research was supported by the National Science Foundation through award Nos. CMS-0304472 and CMS-0120866, and by the US Army Research Office through Grant No. W911NF-05-1-0088. Computing support from the San Diego Supercomputer Center (NPACI resources) is gratefully acknowledged.

References

- [1] Fleck NA, Muller GM, Ashby MF, Hutchinson JW. Strain gradient plasticity: theory and experiment. *Acta Metall Mater* 1994;42:475–87.

- [2] Fleck NA, Hutchinson JW. A phenomenological theory for strain gradient plasticity. *J Mech Phys Solids* 1993;41:1825–57.
- [3] Xiang Y, Vlassak JJ. Bauschinger effect in thin metal films. *Scri Mater* 2005;53:177–82.
- [4] Espinosa HD, Prorok BC. Effects of film thickness on the yielding behavior of polycrystalline gold films. *Mater Res Soc Symp Proc* 2001;695:L8.3.1–6.
- [5] Espinosa HD, Prorok BC, Fischer M. A novel method for measuring elasticity, plasticity and fracture of thin films and MEMS materials. *J Mech Phys Solids* 2003;51:47–67.
- [6] Espinosa HD, Prorok BC, Peng B. Plasticity size effects in free-standing submicron polycrystalline FCC films subjected to pure tension. *J Mech Phys Solids* 2004;52:667–89.
- [7] von Blanckenhagen B, Arzt E, Gumbsch P. Discrete dislocation simulation of plastic deformation in metal thin films. *Acta Mater* 2004;52:773–84.
- [8] Espinosa HD, Berbenni S, Panico M, Schwarz KW. An interpretation of size-scale plasticity in geometrically confined systems. *Proc Natl Acad Sci USA* 2005;102:16933–8.
- [9] Espinosa HD, Panico M, Berbenni S, Schwarz KW. Discrete dislocation dynamics to interpret size and grain boundary effects in free-standing FCC thin films. *Int J Plasticity* 2006;22:2091–117.
- [10] Uchic MD, Dimiduk DM, Florando JN, Nix WD. Sample dimensions influence strength and crystal plasticity. *Science* 2004;305:986–9.
- [11] Dimiduk DM, Uchic MD, Parthasarathy TA. Size-affected single-slip behavior of pure nickel microcrystals. *Acta Mater* 2005;53:4065–77.
- [12] Greer JR, Oliver WC, Nix WD. Size dependence of mechanical properties of gold at the micro scale in the absence of strain gradients. *Acta Mater* 2005;53:1821–30.
- [13] Deshpande VS, Needleman A, Van der Giessen E. Plasticity size effects in tension and compression of single crystals. *J Mech Phys Solids* 2006;53:2661–91.
- [14] Benzerga AA, Shaver NF. Scale dependence of mechanical properties of single crystals under uniform deformation. *Scri Mater* 2005;54:1937–41.
- [15] Schwarz KW. Simulations of dislocations on the mesoscopic scale. I. Methods and examples. *J Appl Phys* 1999;85:108–19.
- [16] Schwarz KW. Local rules for approximating strong dislocation interactions in discrete dislocation dynamics. *Model Simul Mater Sci Eng* 2003;11:609–25.
- [17] Liu XH, Schwarz KW. Modelling of dislocations intersecting a free surface. *Model Simul Mater Sci Eng* 2005;13:1233–47.
- [18] Gilman JJ. *Micromechanics of flow in solids*. New York: McGraw-Hill; 1969.
- [19] Caillard D, Martin JL. *Thermally activated mechanisms in crystal plasticity*. Pergamon Materials Series. Oxford: Elsevier; 2003. p. 339.
- [20] Madec R, Devincere B, Kubin LP, Hoc T, Rodney D. The role of collinear interaction in dislocation-induced hardening. *Science* 2003;301:1879–82.
- [21] Moulin A, Condat M, Kubin LP. Mesoscale modeling of the yield point properties of silicon crystals. *Acta Mater* 1999;47:2879–88.
- [22] Moulin A, Condat M, Kubin LP. Simulation of Frank–Read sources in silicon. *Acta Mater* 1997;45:2339–48.
- [23] Frost HJ, Ashby MF. Motion of a dislocation acted on by a viscous drag through an array of discrete obstacles. *J Appl Phys* 1971;42:5273–9.
- [24] <http://clifton.mech.northwestern.edu/~espinosa/movies/>.
- [25] von Blanckenhagen B, Gumbsch P, Arzt E. Dislocation sources in discrete dislocation simulations of thin-film plasticity and the Hall–Petch relation. *Model Simul Mater Sci Eng* 2001;9:157–69.